Vessel segmentation in high-frequency 2D/3D ultrasound images

Johan Chaniot, Bruno Sciolla, Philippe Delachartre, Thibaut Dambry, Benoît Guibert

Vessel Segmentation in High-Frequency 2D/3D Ultrasound Images

Johan Chaniot, Bruno Sciolla
and Philippe Delachartre
CREATIS laboratory, INSA Lyon, France
Email: bruno.sciolla@creatis.insa-lyon.fr

Thibaut Dambry and Benoît Guibert
Atys Medical
Soucieu-En-Jarrest, France

***Abstract*—Characterizing the microvascular architecture has a wide range of medical and biological applications in the fields of angiology, oncology and dermatology. We propose a method to segment vessels in 2D temporal sequences and in 3D images using high-frequency ultrasound (25-50 MHz). The method takes as input the native ultrasound images, and detects the vessels based the intensity and the dynamical decorrelation. It enables to characterize the vascularization of tumors or organs whenever a Doppler mode is not available.**

I. Introduction

Several medical imaging systems allow to characterize the microvascularization at high resolution, such as Dynamic Contrast Enhanced Magnetic Resonance Imaging [1], or High Resolution Contrast Magnetic Resonance Imaging [2], micro-computed tomography [3], Optical Coherence tomography [4] and Fluorescence Molecular Tomography [5]. Several ultrasound methods have been proposed as well to make high-resolution images of the microvessels, like Acoustic Angiography [6] and Ultrafast ultrasound [7]. Such imaging systems are usually much cheaper and more compact than MRI or optical systems.

In the current work we develop a method to detect vessels in high-frequency ultrasound (25-50 MHz). Due to the small size of high-frequency ultrasound transducers, all systems do not use linear arrays. On most lightweight high-frequency imaging systems, the probe is mechanical and Doppler imaging is not available. We therefore propose an alternative to Doppler imaging which is suitable to characterize vessels. Several previous studies have addressed a similar problem. For example, [8] describes a method to measure flow patterns from sequential images based on the optical flow. Ref. [9] proposes to use Maximum Cross-Correlation to distinguish blood and cardiac tissues according to their temporal decorrelation. In [10], an active contour method is proposed to segment vessels, based on a Fisher-Tippett parametrization of the IQ signal.

We propose a method to detect the vessels applicable to dynamical sequences or 3D images. The algorithm combines two measures to discriminate between the vessels and the surrounding tissues: an intensity-based criterion and a temporal decorrelation-based criterion. Both measures are integrated in a variational framework, which ensures the continuity of the boundary of the vessel, spatially as well as temporally for dynamical sequences. In contrast to the methods [6] and [7], our method is applicable with or without using a contrast agent.

II. Method

A. Data acquisition

Images of the dermis vascularization in the hand are acquired with a Dermcup ultrasound imaging system (Atys Medical, Soucieu-en-Jarrest, France) with a 50 MHz 3D mechanical probe or a 25 MHz 2D probe for dynamical sequences, shown in Fig. 1. The 3D images are obtained with the mechanical probe of the constructor, with a field of view of 16mm $\times$ 16mm $\times$ 3.1mm (last is depth). The size of a voxel is of 53.5μm $\times$ 53.3μm $\times$ 3.7μm. The axial resolution is of 25μm, the lateral resolution of 50μm.

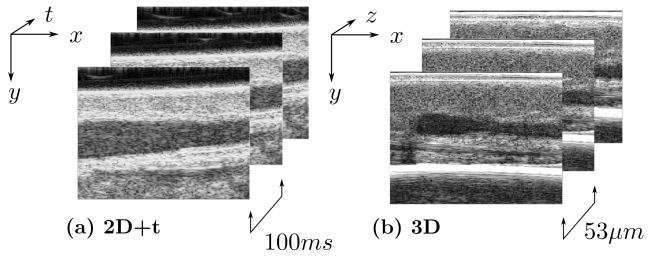

Fig. 1. (a) 2D+t image $I(\mathbf{x})$. The axis z is the time t. There is a delay of 100*ms* between each frame. (b) 3D image $I(\mathbf{x})$. z is the third spatial dimension with a distance of 53μm between frames.

B. Method

Our vessel segmentation algorithm discriminates between tissues and vessels based on two criteria, which are integrated into an active-contours segmentation. Specifically, if $\mathbf{x}$ is a point in the image, we say that $\mathbf{x}$ belongs to A if the point is in the region of the vessel and otherwise that $\mathbf{x}$ belongs to B the background tissue. Our goal is to find the region A with best match to the vessel. In the following, $\mathbf{x} = \{x, y, t\}$ for the dynamical sequences and $\mathbf{x} = \{x, y, z\}$ for 3D images.

1) Intensity criterion: The first criterion discriminates vessels from the (log-envelope) intensity I, under the assumption that vessels are usually hypoechogenic compared with the surrounding tissue - or hyperechogenic whenever a contrast agent is used. Assuming that each point $\mathbf{x}$ with intensity $I(\mathbf{x})$

in region A is an independent variable distributed according to a distribution $P_A(I)$, and according to another distribution $P_B(I)$ in the region B, several methods have been proposed to split the image into two maximally distinct regions A and B [11], [12]. In analogy with Ref. [13], the partition (A, B) with maximum likelihood is chosen. The likelihood of a partition is given by $P = \prod_{\mathbf{x}\in A} P_A(I(\mathbf{x})) \prod_{\mathbf{x}\in B} P_B(I(\mathbf{x}))$, and for computational convenience reasons, it is better to minimize minus the log-likelihood:

$$E^{\text{int}}(A,B) = -\sum_{\mathbf{x}\in A} \log(\widehat{P}_A(I(\mathbf{x}))) - \sum_{\mathbf{x}\in B} \log(\widehat{P}_B(I(\mathbf{x}))) \quad (1)$$

The distributions $\widehat{P}_A(I(\mathbf{x}))$ are estimated directly using histograms (or more specifically, Parzen estimates, like in Ref. [11]) of the actual intensity $I(\mathbf{x})$ for $\mathbf{x} \in A$, and similarly for B.

2) Decorrelation criterion: The second criterion that we use is a temporal decorrelation term, capable of detecting the speckle motion, which is present in the vessels and less prominent in the tissues. In order to treat the temporal and spatial variables differently, we apply a mixed hyperbolic Wavelet Transform [14] to the image. Indeed, since the images are anisotropic in the z directions compared with the $x-y$ planes, as shown in Fig. 2(a), the anisotropic wavelet coefficients are suited to isolate the high frequency signal along the z direction specifically [15]. The transform is defined as $W = \mathscr{W}_z(\mathscr{W}_{xy}(I))$ where $\mathscr{W}_{xy}$ is a stationary isotropic transform with 4-Daubechies wavelets applied on the xy planes and $\mathscr{W}_z$ is a stationary 4-Daubechies wavelet transform applied on the z direction. Figure 2 depicts the spatio-temporal decomposition in the case of a decimated transform for clarity - yet we use a non-decimated (stationary) version here. We define the decorrelation criterion using the high-frequency temporal wavelet h and low frequency spatial components ll: $U = W_{h,ll}$ at first order in recursion, corresponding to a spatial regularization of a high-pass temporal filter. The U coefficients allow to characterize the flow: in regions of tissue the coefficients are mostly zero while in regions of flow the coefficients take a broad range of values. To discriminate between the two, we compute the entropy of the distribution of the coefficients in spatial blocks $\mathscr{B}$ of width $b = 5$ in the $x-y$ plane. Given a bloc $\mathscr{B}_{\mathbf{x}}$ centered around a point $\mathbf{x}$, let us call $P_{\mathscr{B}_{\mathbf{x}}}(U)$ the histograms of wavelet coefficents U in the bloc. The entropy of the coefficients is then given by:

$$\mathscr{S}(\mathbf{x}) = -\sum_U P_{\mathscr{B}_{\mathbf{x}}}(U) \log P_{\mathscr{B}_{\mathbf{x}}}(U) \quad (2)$$

We increase further the contrast between flow and tissue, applying a spatio-temporal mean filtering on the entropy map $\mathscr{S}(\mathbf{x})$ and dividing by a smoothed intensity map:

$$C(\mathbf{x}) = \frac{H_1 * \mathscr{S}}{H_2 * I} \quad (3)$$

with H_1 a Gaussian 3D filter of width $\sigma = 4$ pixels and H_2 a Gaussian 3D filter of width $\sigma = 2$ pixels. We use the resulting contrast map $C(\mathbf{x})$ in a maximum likelihood framework in the same way as the intensity $I(\mathbf{x})$. This allows to define the decorrelation term E^{cor}:

$$E^{\text{cor}}(A,B) = -\sum_{\mathbf{x}\in A} \log(\widehat{P}_A(C(\mathbf{x}))) - \sum_{\mathbf{x}\in B} \log(\widehat{P}_B(C(\mathbf{x}))) \quad (4)$$

with new density distributions $\widehat{P}_A(C)$, $\widehat{P}_B(C)$ obtained via Parzen estimates as before.

Figure 3 shows an in-vivo image of a vessel and the different distributions of the intensity I in the vessel and in the tissue, as well as the entropy map C. Figure 3(b) and (d) show that both the intensity and the entropy map are good discriminative features to distinguish the vessel and tissues.

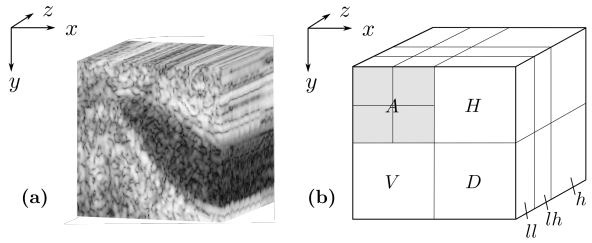

Fig. 2. **(a)** 2D temporal sequence represented as a 3D bloc. The signal is very anisotropic in the z direction because the tissue is not moving. In contrast, in the vessel the speckle has a fast motion. **(b)** Hyperbolic wavelet coefficients. The transform is an isotropic wavelet transform in the $x-y$ direction with for quadrants (approximation coefficients A, horizontal details H, vertical details V, diagonal details D). The decomposition at the second level is illustrated with lines. Along the z direction, the h are the details coefficients at the first level of recursion, lh the details at the the second level and ll the approximation coefficients.

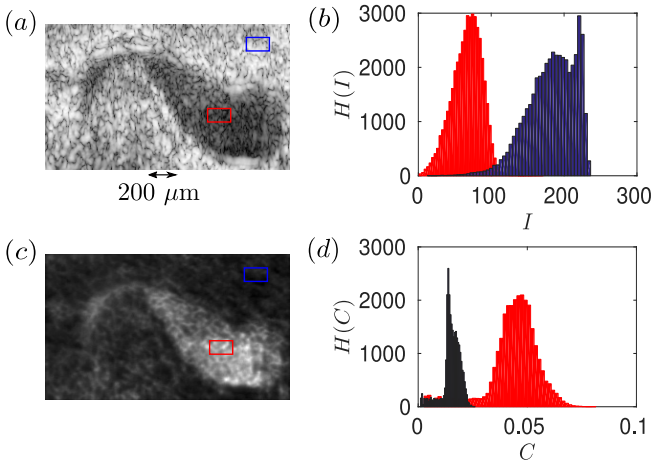

Fig. 3. (a) 2D in-vivo image $I(\mathbf{x})$ of an artery of the wrist at 25MHz. (b) Histograms of the intensity I in the vessel area (red) and in the tissue (blue), cumulated on all the temporal sequence. (c) Smoothed entropy map $C(\mathbf{x})$ (d) Histograms of the entropy map C in the vessel (red) and tissue (blue).

3) Active contour: The two criteria above are combined in a variational active contour framework:

$$E(A,B) = \alpha E^{\text{int}}(A,B) + \beta E^{\text{cor}}(A,B) + \gamma E^{\text{reg}}(A,B) \quad (5)$$

where $E^{\text{reg}}(A,B)$ is a regularization term equal to the perimeter of region A in 2D and to the surface of region A in 3D.

1: User initialization of region A
2: **while** A not converged **do**
3: Compute $\widehat{P}_A(I)$, $\widehat{P}_B(I)$, $\widehat{P}_A(C)$, $\widehat{P}_B(C)$
4: Update region A via a gradient descent step for (5)
5: **end while**

Fig. 4. Active contour algorithm. The gradient descent is assumed to have converged when the area A is changed by less than 0.01% during a step.

This term ensures that the region A has smooth and regular boundaries. The active contour is implemented using a level-set implicit representation of the contour, which allows to minimize the energy (5) by gradient descent with a solver similar to Ref. [16]. The algorithm is summarized in Fig. 4.

III. Results

Our method is tested on a synthetic 2D sequence and on in-vivo acquisitions.

A. Numerical simulation

The synthetic images are obtained from a simple response model assuming a constant impulse response h across the medium [13]. This assumption is usually not valid for the whole images, but is reasonable if the synthetic image is used only to simulate vessels placed in the vicinity of the focal zone, for example in the range of depth 3-6mm at 25MHz. We assume that the imaged region contains N scatterers of amplitude ρ_i placed at position $\{x_i, y_i, z_i\}$, with $i = 1, \ldots, N$. The scatterers ρ_i are drawn at random according with a density given by a background profile shown in Fig. 5(a). We define a complex scatterers map s with

$$s(x,y,z) = \sum_{i=1}^{N} \rho_i \delta_{x,\lfloor x_i \rfloor} \delta_{y,\lfloor y_i \rfloor} \delta_{z,\lfloor z_i \rfloor} e^{2iy_i k} \tag{6}$$

where $x = 1, \ldots, L_x$, $y = 1, \ldots, L_y$, $z = 1, \ldots, L_z$ are integers labeling the spatial coordinates. $\lfloor . \rfloor$ denotes the floor function, $k = 2\pi/\lambda$ is the wavenumber of the ultrasound wave and λ its wavelength. With this scattering map, the received envelope signal is modeled as

$$E(\mathbf{x}) = |f(x,z) f^e(y) * s| \tag{7}$$

where $*$ is the convolution along the 3 directions x, y, z. $f(x,z)$ is an effective spatial response model, and $f^e(y)$ is the effective enveloppe profile in the direction of the propagation. The rationale behind this model is that in the limit of a large scatterers density, the envelope follows a Rayleigh distribution. Like in more realistic simulations such as Field II [17] or Creanuis [18], a vertical displacement of a scatterer introduces a phase shift. In the simulations, $f(x,z)$ is a cardinal sine and $f^e(y)$ is a Gaussian packet.

In order to simulate motion, the position of the scatterers is updated $\{x_i(t), y_i(t), z_i(t)\}$ and the new scattering map is computed according to (6).

The 2D synthetic images are obtained as a slice of a 3D envelope map computed on a thin 3D scatterers map for a realistic rendering. Temporal 2D sequences are obtained as repeated simulations with the time-dependent scatterers map (6).

Figure 5(b) shows a frame of a realistic simulated 2D sequence with inhomogeneous background tissues. The segmented vessel closely matches the .

The accuracy is measured using the Mean Absolute Distance (MAD) and Dice coefficient. We call ∂A the boundary of the segmented vessel, $N_{\partial A}$ the number of voxels in ∂A, and R the manual contouring of the vessel (reference). Let $d_i^{\partial A \leftrightarrow R}$ be the shorter distance between the i-th voxel in the boundary ∂A to any voxel in the reference R. The MAD is defined as $\text{MAD} = \frac{1}{N_{\partial A}} \sum_{i=1}^{N_{\partial A}} d_i^{\partial A \leftrightarrow R}$. The Dice coefficient is a measure of the overlap between the segmented area A and the reference R, defined as $D = 2N_{A \cap R}/(N_A + N_R)$ where $\cap$ is the (set theory) intersection and $N_\star$ denotes the number of voxels in the region $\star$.

The agreement between the two is excellent, with a Dice coefficient of 0.97 and a Mean Absolute Distance of 2.0 pixels, or $100\mu m$.

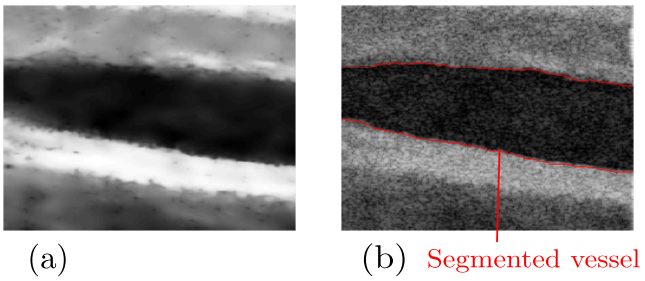

Fig. 5. **(a)** Slice of the 3D map from which random scatterers are drawn. **(b)** Synthetic image drawn according to (7). The segmented vessel is shown in red.

The method is also tested on in-vivo 2D images of an artery in the wrist at 25MHz. Fig. 6 shows the segmented vessel and the same after 0.5 s. Because the vessel is curved on the left, it goes out of plane and appears in one or two pieces in the slice, due to the artery beating motion. Notice that the current method is robust to topological changes and correctly segments the vessel across the whole sequence.

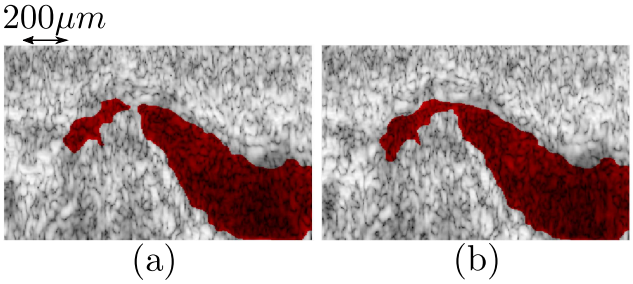

Fig. 6. Segmented flow (red area) in a 2D sequence of a wrist artery at 25 MHz. (a) The segmented vessel, (b) the same after 0.5 s.

Finally the method is tested on in-vivo 3D images of the finger at 50MHz. The segmented vascular network is shown in figure 7. Due to attenuation, the bottom of the segmented

region contains hypoechogenic regions which are not vessels.

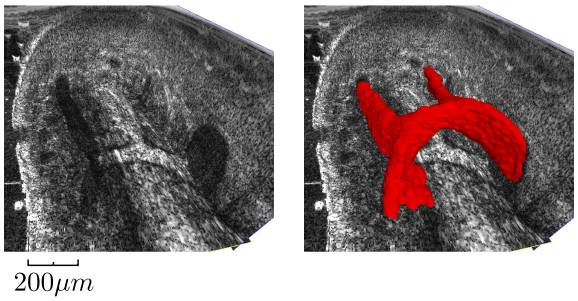

Fig. 7. Segmentation of a vascular branching in the thumb on a 3D ultrasound image at 50MHz.

Qualitatively, we have observed that the method has the following properties:

- Very contrasted vessels are easier to segment than vessels in a background of hypoechogenic tissues.
- The segmentation of vessels has better accuracy in 2D dynamical images than in 3D images. Indeed, as depicted in Fig. 1, in 2D dynamical sequences, the decorrelation in the z direction is only due to motion, and there is only motion in the vessels. On the contrary, in 3D images, a spatial decorrelation is present along the z direction, in addition to the temporal decorrelation. This reduces the discriminate power of the decorrelation term, making 3D vessel segmentation a harder task than 2D dynamical vessel segmentation.

IV. Conclusion

We have described an algorithm for the segmentation of vessels in dynamical high-frequency ultrasound dynamical sequences or 3D images. The algorithm detects the vessels based on an intensity criterion and on a decorrelation criterion computed via the hyperbolic wavelet transform. Such a method is relevant for high-frequency imaging systems without a Doppler mode, where it could play a similar role for the operator, to estimate the vascularization of tissues such as tumors or organs. A significant advantage of this method is its simplicity and versatility. Because it is a post-processing algorithm, it requires no specific imaging system or imaging sequence.

Acknowledgment

This work was funded by the ANR-14-LAB3-0006-01 LabCom AtysCrea and was supported by the LABEX CeLyA (ANR-10-LABX-0060) of Université de Lyon, within the "Investissements d'Avenir" program (ANR-11-IDEX-0007) operated by the French National Research Agency (ANR).

References

[1] A. R. Padhani, K. A. Krohn, J. S. Lewis, and M. Alber, "Imaging oxygenation of human tumours," *European Radiology*, vol. 17, no. 4, pp. 861–872, 2007. [Online]. Available: http://dx.doi.org/10.1007/s00330-006-0431-y

[2] R. T. Ullrich, J. F. Jikeli, M. Diedenhofen, P. Bhm-Sturm, M. Unruh, S. Vollmar, and M. Hoehn, "In-vivo visualization of tumor microvessel density and response to anti-angiogenic treatment by high resolution mri in mice," *PLoS ONE*, vol. 6, no. 5, pp. 1–7, 05 2011.

[3] R. Savai, A. C. Langheinrich, R. T. Schermuly, S. S. Pullamsetti, R. Dumitrascu, H. Traupe, W. S. Rau, W. Seeger, F. Grimminger, and G. A. Banat, "Evaluation of angiogenesis using micro-computed tomography in a xenograft mouse model of lung cancer," *Neoplasia*, vol. 11, no. 1, pp. 48–56, 2009.

[4] B. J. Vakoc, D. Fukumura, R. K. Jain, and B. E. Bouma, "Cancer imaging by optical coherence tomography: preclinical progress and clinical potential," *Nature Reviews Cancer*, vol. 12, no. 5, pp. 363–368, 2012.

[5] X. Montet, J.-L. Figueiredo, H. Alencar, V. Ntziachristos, U. Mahmood, and R. Weissleder, "Tomographic fluorescence imaging of tumor vascular volume in mice 1," *Radiology*, vol. 242, no. 3, pp. 751–758, 2007.

[6] R. C. Gessner, C. B. Frederick, F. S. Foster, and P. A. Dayton, "Acoustic angiography: a new imaging modality for assessing microvasculature architecture," *Journal of Biomedical Imaging*, vol. 2013, p. 14, 2013.

[7] C. Errico, J. Pierre, S. Pezet, Y. Desailly, Z. Lenkei, O. Couture, and M. Tanter, "Ultrafast ultrasound localization microscopy for deep super-resolution vascular imaging," *Nature*, vol. 527, no. 7579, pp. 499–502, 2015.

[8] J. H. Lee, Y. N. Hwang, S. Y. Park, J. S. Jeong, and S. M. Kim, "An analysis of contrast agent flow patterns from sequential ultrasound images using a motion estimation algorithm based on optical flow patterns," *IEEE Transactions on Biomedical Engineering*, vol. 62, no. 1, pp. 49–59, 2015.

[9] A. E. Saris, M. M. Nillesen, R. G. Lopata, and C. L. de Korte, "Correlation-based discrimination between cardiac tissue and blood for segmentation of the left ventricle in 3-d echocardiographic images," *Ultrasound in medicine & biology*, vol. 40, no. 3, pp. 596–610, 2014.

[10] G. Slabaugh, G. Unal, T. Fang, and M. Wels, "Ultrasound-specific segmentation via decorrelation and statistical region-based active contours," in *2006 IEEE Computer Society Conference on Computer Vision and Pattern Recognition (CVPR'06)*, vol. 1. IEEE, 2006, pp. 45–53.

[11] O. Michailovich, Y. Rathi, and A. Tannenbaum, "Image segmentation using active contours driven by the Bhattacharyya gradient flow," *Image Processing, IEEE Transactions on*, vol. 16, no. 11, pp. 2787–2801, Nov 2007.

[12] J. Kim, J. Fisher, A. Yezzi, M. Cetin, and A. Willsky, "A nonparametric statistical method for image segmentation using information theory and curve evolution," *Image Processing, IEEE Transactions on*, vol. 14, no. 10, pp. 1486–1502, Oct 2005.

[13] B. Sciolla, P. Ceccato, L. Cowell, T. Dambry, B. Guibert, and P. Delachartre, "Segmentation of inhomogeneous skin tissues in high-frequency 3d ultrasound images, the advantage of non-parametric log-likelihood methods," *Physics Procedia*, vol. 70, pp. 1177–1180, 2015.

[14] Y. Farouj, J.-M. Freyermuth, L. Navarro, M. Clausel, and P. Delachartre, "Hyperbolic Wavelet-Fisz denoising for a model arising in Ultrasound Imaging," Feb. 2016, working paper or preprint. [Online]. Available: https://hal.archives-ouvertes.fr/hal-01322246

[15] S. G. Roux, M. Clausel, B. Vedel, S. Jaffard, and P. Abry, "Self-similar anisotropic texture analysis: The hyperbolic wavelet transform contribution," *IEEE Transactions on Image Processing*, vol. 22, no. 11, pp. 4353–4363, 2013.

[16] B. Sciolla, L. Cowell, T. Dambry, B. Guibert, and P. Delachartre, "Segmentation of skin tumors in high-frequency 3D ultrasound images," *Ultrasound in medicine & biology, in press*, 2016.

[17] J. A. Jensen, "Simulation of advanced ultrasound systems using field II," in *Biomedical Imaging: Nano to Macro, 2004. IEEE International Symposium on*. IEEE, 2004, pp. 636–639.

[18] F. Varray, O. Basset, P. Tortoli, and C. Cachard, "Creanuis: A non-linear radiofrequency ultrasound image simulator," *Ultrasound in Medicine & Biology*, vol. 39, no. 10, pp. 1915 – 1924, 2013.